Tracking the Adaptation and Compensation Processes of Patients' Brain Arterial Network to an Evolving Glioblastoma

Junxi Zhu[®], Spencer Teolis, Nadia Biassou, Amy Tabb[®], Pierre-Emmanuel Jabin[®], and Orit Lavi[®]

Abstract—The brain's vascular network dynamically affects its development and core functions. It rapidly responds to abnormal conditions by adjusting properties of the network, aiding stabilization and regulation of brain activities. Tracking prominent arterial changes has clear clinical and surgical advantages. However, the arterial network functions as a system; thus, local changes may imply global compensatory effects that could impact the dynamic progression of a disease. We developed automated personalized system-level analysis methods of the compensatory arterial changes and mean blood flow behavior from a patient's clinical images. By applying our approach to data from a patient with aggressive brain cancer compared with healthy individuals, we found unique spatiotemporal patterns of the arterial network that could assist in predicting the evolution of glioblastoma over time. Our personalized approach provides a valuable analysis tool that could augment current clinical assessments of the progression of glioblastoma and other neurological disorders affecting the brain.

Index Terms—Brain arterial network, adaptation, GBM, patient data, network topology and hemodynamics

NOMENCLATURE

ACA Anterior cerebral artery

CoW Circle of Willis GBM Glioblastoma

HGG High grade glioblastoma
LGG Low grade glioblastoma
LPCA Left posterior cerebral artery
LMCA Left middle cerebral artery
MCA Middle cerebral artery

MRA Magnetic resonance angiography MRI Magnetic resonance imaging RMCA Right middle cerebral artery RPCA Right posterior cerebral artery

1 Introduction

BRAIN diseases come in many different forms. The development of diverse pathological states, though initiated by a distinct set of molecular changes, heavily depends on, and is regulated by a subset of essential interconnected sub-systems

- Junxi Zhu, Spencer Teolis, and Orit Lavi are with Integrative Cancer Dynamics Unit, Laboratory of Cell Biology, CCR, NCI, NIH, Bethesda, MD 20892 USA. E-mail: {junxi.zhu, spencer.teolis, orit.lavi}@nih.gov.
- Pierre-Emmanuel Jabin is with the Department of Mathematics, University of Maryland, College Park, MD 20742 USA. E-mail: pjabin@cscamm.umd.edu.
- Nadia Biassou is with the National Institute of Health Clinical Center, Bethesda, MD 20814 USA. E-mail: biassoun@cc.nih.gov.
- Amy Tabb is with Agricultural Research Service, U.S. Department of Agriculture, Washington, DC 20250 USA. E-mail: amy.tabb@usda.gov.

Manuscript received 19 Oct. 2019; revised 1 July 2020; accepted 1 July 2020. Date of publication 9 July 2020; date of current version 3 Dec. 2021. (Corresponding author: Orit Lavi.)

Recommended for acceptance by G. Carneiro.

Digital Object Identifier no. 10.1109/TPAMI.2020.3008379

that together constitute the complex brain core system. Addressing 'disease conditions' by estimating the repertoire of behaviors of each essential sub-system that would be perturbed or evolve over time could deepen our understanding of a disease's evolution, resulting in a better process of offering treatments and assessing their effectiveness. The greater the dependency of the disease on related brain components, the greater the need for a system-level view [1], [2].

One such vital sub-system is the human brain arterial network [3]. Its critical unique function is to fulfill the brain's constant high metabolic demands, as significant changes in oxygen level may result in permanent damage or even neuronal cell death. Thus, the arterial network must function as a robust system [4]. However, its centrality is also demonstrated by its connections to all other solid, soft, and fluid components that together constitute the brain [5]. Such central characteristics can easily have an impact on and be affected by other systems or conditions such as tumors or surgery. Thus, the arterial network must also be adaptive. An essential complex system such as the arterial network includes key processes to guarantee its functional and structural stability, e.g., autoregulation or adaptation, which could both contribute to compensation for inefficiencies or abnormalities [3]. Autoregulation and adaption cause changes in the arterial network topology, resulting in functional blood flow variations [6]. Although it is well known that both processes are important to guarantee a functioning arterial network, it is unknown which circumstances or disease conditions induce one process more than the other. The timing and extent of changes an arterial network undergoes over time, in response to a certain disease, have not yet been thoroughly mapped.

In this study, we addressed this question of how the brain arterial network adapts over the course of a disease.

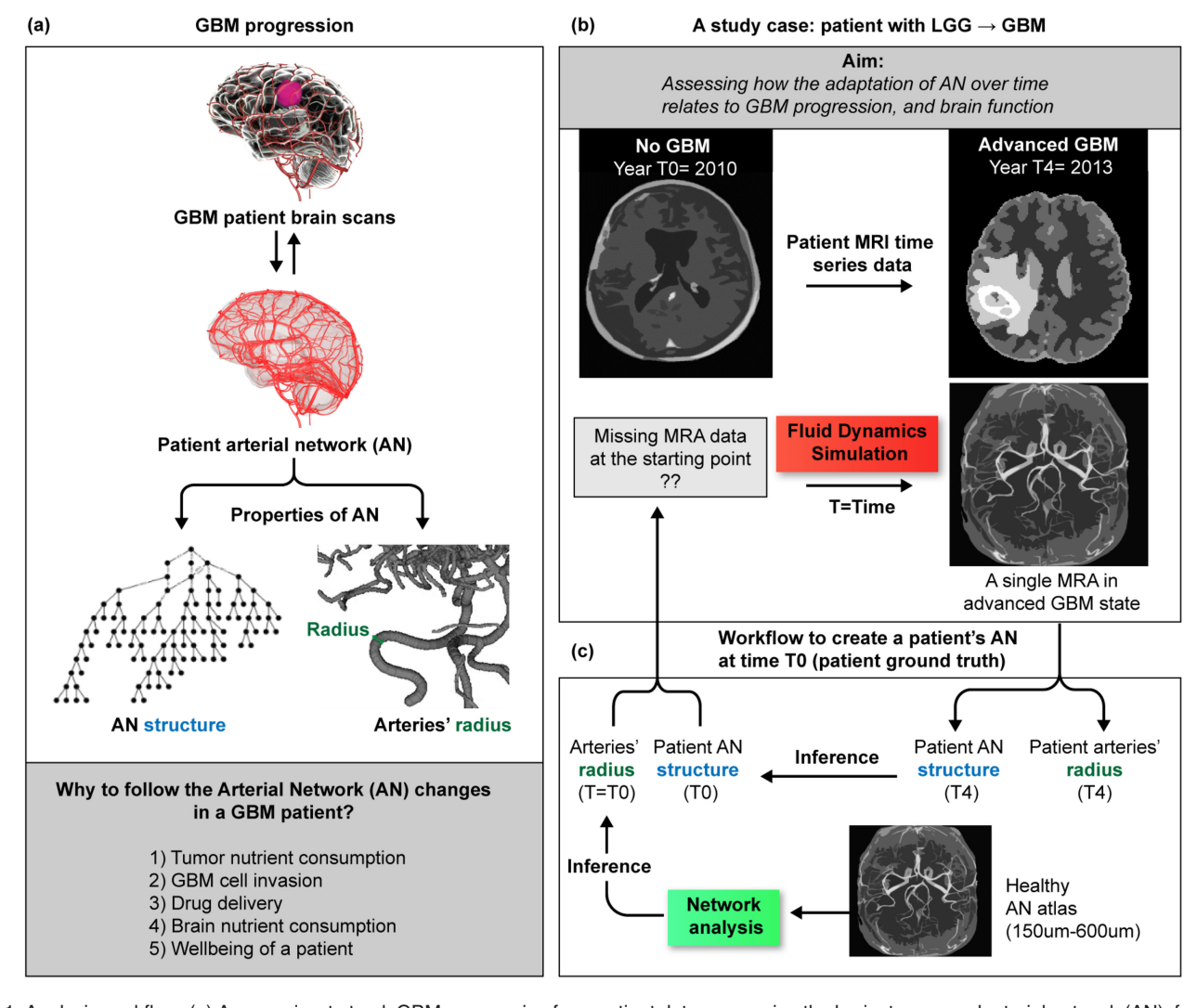


Fig. 1. Analysis workflow. (a) An overview to track GBM progression from patient data concerning the brain, tumor, and arterial network (AN), from an image to a detailed network with all of its properties. The arterial network mainly includes its structure and the radius length of each branch. (b) A study of a specific GBM patient with time series MRI data, with a single MRA at an advanced stage of GBM. The aim is to assess how the AN adaptation over a period of time is related to GBM progression and brain function, using fluid dynamics simulation. (d) Since normally there is no MRA scan during the initial development of the disease, we propose a method to infer the configuration of the patient's AN. Such a method includes creating a healthy AN atlas from a range of resolutions (150 μ m-600 μ m), and its network analysis results in order to infer the properties of a patient's AN.

We started by developing automated personalized systemlevel methods to track and analyze the structure of a patient's complete brain arterial network, and to estimate its mean blood flow behavior, from magnetic resonance (MR) images. The effects of treatments (such as chemotherapy or radiation), and brain disease progression, not only perturb the arterial network, but also add uncertainties to an image, making it challenging to extract information. Moreover, clinical image datasets are generated from different image resolutions. Thus, it is important to establish which of the arteries' abnormalities are the results of the disease itself, as opposed to other causes. We studied the effects of different image resolutions by comparing two datasets of healthy subjects [7], [8], [9], and exploring their neurovascular structurefunction relationships. Moreover, we address several clinically relevant questions using our approach. In this study, we addressed the question of how the brain arterial network adapts over the course of a disease. We started by developing automated personalized system level methods to track and analyze the structure of a patient's complete brain arterial network, and to estimate its mean blood flow behavior, from magnetic resonance images. The main issue in studying dynamic processes in cancer is the lack of patient time series data, especially during the initial developmental period of the disease. To estimate the patient's arterial network during the non-GBM stage, a creative approach was needed. We needed to create an atlas of a healthy brain arterial network from a range of image resolutions (150 μ m-600 μ m) and infer the initial configuration of the patient's arterial network. A workflow image is provided in Fig. 1.

Having such an atlas could help to resolve many issues. The effects of treatments (such as chemotherapy or radiation), and brain disease progression, not only perturb the arterial network, but also add uncertainties to an image, making it challenging to extract information. Moreover, clinical image datasets are generated at different image resolutions. Thus, it is important to establish which of the arteries' abnormalities are the results of the disease itself, as opposed to other causes. We studied the effects of different image resolutions by comparing two datasets of healthy

subjects [7], [8], [9], and exploring their neurovascular structure-function relationships. Altogether, our method can extract information from a patient's images, and address challenging questions in cases of missing data by comparing them to the healthy atlas or another source, if needed.

By analyzing time series data from a patient with aggressive brain cancer, we found significant variations in the structure of the arterial network, and the resulting changes in blood flow dynamics due to biomechanical mechanism. We simulated the evolution in the patient's arterial network over time and find that the patient's arterial network changes are due to the interplay between the development of the tumor and compensation processes of the brain. We show that significant disease-related local changes cause global changes at the arterial network, which in return impacts the progression of the disease. Our automated methodframework could easily be applied to large cohort of patients, perform statistical analyses that reliably identify markers of glioblastoma (GBM) or other neurological disorders affecting the brain. Moreover, it provides a valuable personalized assessment analysis that could complement the current clinical approach.

2 MATERIALS AND METHODS

2.1 Experimental Design

The methods of our study can be divided into two important steps. First, we elaborate on methods to segment and construct graphs from human MR image data, which include 1) raw image registration, 2) vesselness filtering, 3) skeletonization, 4) manual error correction, 5) graph representation. Second, we estimate the steady-state fluid flow behavior of a given arterial network using a 1D model that is suitable when patient brain fluid flow data is lacking.

2.2 Data Availability

Our source code can be fully and freely downloaded from project GitHub page (https://github.com/zjx1805/ArteryNetwork) or https://github.com/OritLavi/Artery Network.

2.3 Datasets

Four cohorts of datasets were used in this study. First, we analyzed data gathered by Speck et al., who imaged a healthy brain arterial network at high resolution. It consists of T1-weighted whole brain anatomical data acquired at 7 Tesla with a nominal isotropic resolution of 250 μ m [8], and 150 μ m MR angiography (MRA) [7] that focused on the middle portion of the brain, of a single young healthy Caucasian subject, recorded using prospective motion correction. We studied the structural properties of this arterial network. Second, we worked with data from Wright et al., [9] who imaged and studied the brain arterial network of 61 healthy subjects with 3T time-of-flight MRA images (with a 620 μ m isotropic resolution). Of the 61 subjects, 36 were females and 25 males, with an average age of 31.2 \pm 10.7 and a range of 19-64 years. Reconstruction of the six major arterial trees, left and right middle cerebral arteries (MCAs), posterior cerebral arteries (PCAs), and anterior cerebral arteries (ACAs), starting at the Circle of Willis (CoW) for each subject. We compared the arterial network properties at two image resolutions, using the Speck and Wright datasets. Third, to address fluid flow behavior, Blanco et al. [10] developed an anatomically detailed arterial network (ADAN) model. Their entire dataset was established based on the literature and known autopsy results, but not from patient image data. It consists of more than 2,000 vessels with well-established branches over the entire human body, with about 140 vessels in the brain. They provided 1D flow simulation results (pressure and flow rate waveform for one cardiac cycle) for each of the vessel branches obtained by solving the 1D Navier-Stokes equation (see Appendix C), which can be found on the Computer Society Digital Library at http://doi. ieeecomputersociety.org/10.1109/TPAMI.2020.3008379. The fourth dataset consists of a GBM image data with clinical information from NIH (BTRIS 2018 1358 LAVI O NCI), including 400 GBM patients with MRI Brain-Perfusion data. For 8 patients there is also information concerning brain arteries, although only a single patient had a full brain MRA performed. That patient was a female in her early 30s who came to the NIH in 2010 with LGG that two years later, transformed into GBM. A summary of the scan parameters of the four datasets and their corresponding usage throughout the paper is shown in Table S1, available in the online supplemental material.

2.4 Raw Image Registration

Two sets of 3D MRI images (250 μm and 150 μm) of the same healthy patient but with different coverage were obtained by Hendrik et~al.~ [7] The sequence parameters for the two acquisitions are: TR=50/35 ms (for 250 μm and 150 μm data, respectively), TE=6.63/6.63 ms, flip angle=25/23 degrees, FOV=196 \times 147 \times 78/196 \times 147 \times 46.8 mm³. Then the two sets of MR images were merged using the nonlinear image registration algorithm in FSL [11], [12], [13], [14] with 12 DoF to form a merged volume. The nonlinear image registration algorithm in FSL [11], [12], [13], [14] with 12 DoF is used to register multiple MR images of different time points, if any, to the same space.

2.5 Vascular Filtering

The merged 150 μ m/250 μ m image wasThe registered images were then filtered using Frangi vascular filter method [15] provided in the vascular modeling toolkit in 3D Slicer [16]. After thresholding, the resulted image was then split into several connected components by a labeling algorithm [17] and each component was fed to a variational region growing technique [18] as an initial attempt to further smooth the boundary of the segmented vessels. There are also more advanced vessel segmentation methods available, such as [19], [20], [21].

2.6 Skeletonization

A curve skeletonization algorithm developed by Tabb and Medeiros [22] specifically designed to deal with elongated objects was applied to the segmented vessel volume from the previous step to extract the centerline of each vessel branch. In order to suppress the spurious vessel segments in noisy regions, the user-defined acceptance probability t was set to $1e^{-12}$.

2.7 Manual Error Correction

It is clear that the resulting skeleton of vessel branches from the previous automatic steps might contain some errors in mis-segmentations due to poor image quality in those regions or due to identification errors. These inaccuracies in connections/segmentations are usually quite difficult to identify automatically, and thus a semi-automated cleaning process using a GUI was performed to manually correct them. Generally, this manual correction step takes less than a minute per mislabeled connection. The GUI program is written in Python and utilizes PyQt to create the interface. Since the arterial network is constructed from the patient's image, not all branches are necessarily connected. Note, analyses reported here include only the results of the connected network. There are some automatic algorithms to fix the disconnected branches, such as [23]. Note that the skeletonization algorithm finds paths to neighboring regions, if there is a path in the segmentation. The problem is not necessarily the skeletonization method, but also resolution and errors in the segmentation, which exist in every domain. If there is not a path in the segmentation, some automatical methods may not connect centerlines.

2.8 Graph Representation

The extracted centerlines of each vessel from the previous steps were converted into a graph representation in which each node corresponds to a bifurcation point/terminating point and each edge corresponds to the centerline of a vessel branch. The radius and length information are embedded in the edges as graph attributes. The purpose of the graph representation of the arterial network is to enable further analysis about its structural properties, e.g., the behavior at the bifurcating point, the distribution of the network properties, the classification of the vessel branches based on brain geometry (e.g., left middle cerebral arteries (LMCAs), right middle cerebral arteries (RMCAs), anterior cerebral arteries, left posterior cerebral arteries (LPCAs), right posterior cerebral arteries (RPCAs)) or physical/functional brain compartments. Except from the arteries in these five major compartments, the graph also contains several major arteries in the neck that supplies blood flow to the entire brain. Also, graph representation enabled us to develop fluid flow modeling.

Several morphological properties of the graph structure are calculated as followsSome researches have shown that vascular morphometrics have some clinical indications [24], [25], [26], [27], [28], [29], [30], [31], and thus several morphological properties of the graph structure are calculated as follows: a vessel branch is referred to as a sequence of centerline points of a specific vessel segmentbranch that starts from a bifurcation point (or root) and ends at another bifurcation point (or termination point). The path length is the geodesic distance between the starting and ending point of a branch. The branch order is the number of the bifurcation point in a branch from the CoWCircle of Willis[32]. The tortuosity is defined as the ratio between the path length and the euclidean (straight) distance of a branch. Two types of properties are measured at each bifurcation point: the local and the remote. The local/ remote bifurcating amplitude is the angle between the bifurcation point and the first/last centerline point of the two branches away from the bifurcation. The (remote) bifurcation tilt is the smaller of the two angles between the bifurcation point, the previous bifurcation towards the current bifurcation, and each of the last centerline points of the two branches away from the current bifurcation. The *torque* is the angle between the plane of the current bifurcation and the plane of the previous bifurcation. Definitions of more morphological properties can be found at the L-Measure website (http://krasnow1.gmu.edu/cn3/) [33].

To identify changes that could infer or indicate accumulating adaptation and compensation changes due to underlying diseases, we studied the graph's properties based on spatial, in addition to non-spatial constraints. Throughout the study, space is included in several interconnected ways (Fig. 2): 1) brain spatial compartments, as posterior versus anterior versus central, or left versus right (Fig. 2d), 2) brain spatial cubic mesh to calculate e.g., artery volume density, or branch density per mesh unit, 3) graph properties (Fig. 2e) that measure its shape (e.g., curvature, angle) of the branches, and the relationship between parents and children bifurcating nodes in a graph, such as tortuosity, amplitude, tilt, and torque.

Moreover, Murray's law predicts the *thickness of branches* in transport networks, such that the cost for transport and maintenance of the transport medium is minimized. Murray's law [34] was tested with two quantities: $(r_1^3 + r_2^3)/r_0^3$ and $(r_1^2 + r_2^2)/r_0^2$, where r_1 and r_2 are radii of child branches and r_0 is the radius of the parent branch. In practice, a power of two, instead of three, is commonly used in different studies [35].

2.9 Fluid Simulation

We provide a method that would work with a minimum amount of data, similar to what is available with the standard-of-care treatment. Thus, we used a simple 1D model, because it requires significantly fewer assumptions, less time and less parameter fitting as compared with the 3D counterpart and yet is still able to provide important information (steady state values). The simplicity refers to the fluid simulation as 1D steady state, instead of more advanced 3D dynamic solutions that are used in other studies. We simulated the steady state solution of a simple model using the type of Hazen-Williams (H-W) equation with the following formula:

$$\Delta P_i = P_{head,i} - P_{tail,i} = \frac{10.67 \cdot Q_i^{k_i}}{c_i^{k_i} \cdot d_i^{4.8704}} \cdot L_i, \tag{1}$$

$$Q_i = v_i \cdot \frac{\pi}{4} \cdot d_i^2, \tag{2}$$

where $c_i, k_i, v_i, d_i, L_i, Q_i, \Delta P_i$ are the roughness coefficient, flow exponent, flow velocity, diameter, length, flow rate and pressure drop of the ith branch (see details in Table S2), available in the online supplemental material. The definition of flow velocity, diameter, length, flow rate are rather self-explanatory, while the roughness coefficient c can be viewed as a proportionality constant coming from the original H-W type relationship: $v = c \times r^{0.63} \times s^{0.54}$, where s is the pressure drop per unit length. The flow exponent k, on the other hand, is taken to be 1.852 in the original H-W type relationship but only works for water. In our model, however, we allow k to have some other value so that it can better fit the

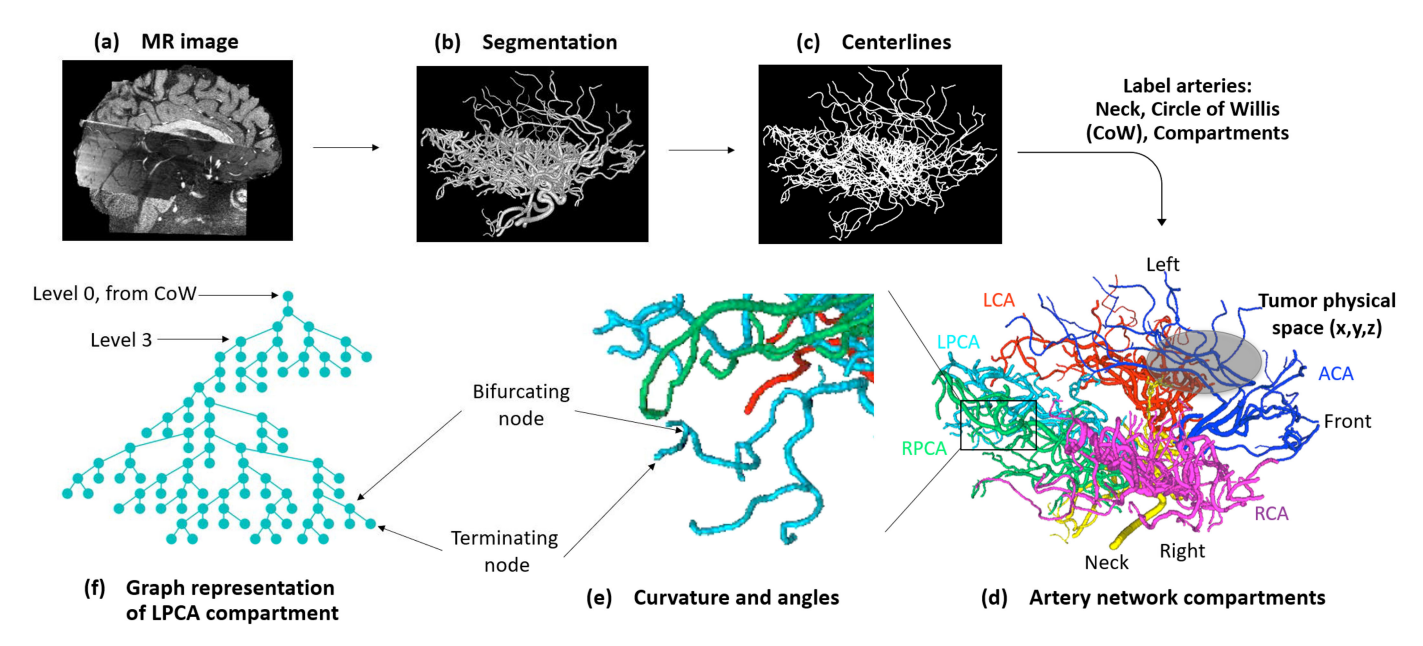


Fig. 2. Workflow of the analysis procedure. (A) MR images of different time or coverage (if any) are registered to the same space. (B) Artery network is segmented from the registered image. (C) Segmented artery network is skeletonized to obtain the centerlines. (D) Five major compartments (LMCA/RMCA/ACA/LPCA/RPCA) are identified and labeled. (E) Various structural properties (e.g., angles and curvatures) are computed for each compartment. (F) The sub-network in each compartment is converted into a graph for further analysis. Extracting properties of a patient's arterial network from MR images. (a) Time series of patient MRIs are used to demonstrate tumor and surgical locations. MR images of different time or coverage (if any) are registered to the same space. (b) The brain arterial network is segmented from the registered image. (c) Segmented arterial network is skeletonized to obtain the centerlines. (d) Five major compartments (LMCA/RMCA/ACA/LPCA/RPCA), the neck and Circle of Willis (CoW) are identified and labeled. (e) Various structural properties (e.g., angles and curvatures) are computed for each compartment. (f) The sub-network in each compartment is converted into a graph for further analysis and for fluid dynamics simulations.

blood flow. In our case for blood flow, it was calculated based on an optimization approach, to better fit the ADAN result.

At each bifurcation node, the incoming flow is equal to the outgoing flow by satisfying the following equation:

$$\sum_{i} Q_{in,i} = \sum_{j} Q_{out,j},\tag{3}$$

where $Q_{in,i}$ and $Q_{out,j}$ represent the flow rate of the *i*th/ jth branch that flows into/out of the bifurcation node. The flow velocities as well as pressures at each bifurcation node are treated as unknown and solved simultaneously through a system of coupled equations consisting of the aforementioned pressure and flow rate conservation relationships. Using the H-W type relationship to approximate the 1D blood flow simulation obtained by solving 1D partial differential equations (PDEs) has both advantages and disadvantages: solving the H-W type relationship is much simpler than solving the PDEs and the relationship does not depend on the Reynolds number. However, it does not account for the viscosity of the blood and assumes a constant radius and flow rate in each branch, which is not the case for actual blood flow. We showed (Appendix C), available in the online supplemental material, that the H-W type relationship is able to reproduce, to a reasonable extent, the pressure predicted by solving the 1D PDEs.

In order to determine the c and k value in the pressure equation, we utilized the 1D fluid simulation results from the ADAN model [10]. We took the average value of the pressure and flow rate waveform and used that as the steady state solution of their results. We chose two major arterial trees on one side (LMCAs+RMCAs, which both

starts from the CoW) in their dataset and ran an optimization to find the best c and k value such that the error between the simulated pressure and their reported pressure at each bifurcating node was minimal. Specifically, we categorized all the branches into 4 groups based on their radii. The branches in one group shared the same roughness coefficient c that was specific to that group. All the branches shared the same flow exponent k. The values of the bin edges uniformly span from the minimum radius of all the segments in LMCA and RMCA to the maximum radius of these segments. For LICA, RICA and BA, if their radius is larger than the maximum radius, then it uses the c and k value of the largest bin. For each set of c and kparameters, a system of equations made up of applying the H-W type relationship to each branch and volume conservation to each bifurcation node were established and solved, the resulting simulated pressures at all the bifurcation nodes were compared to the corresponding predicted pressures from the ADAN result. The optimization process iteratively updated the set of c and k parameters such that the difference between predicted pressures from our dataset and the ADAN dataset became minimal. Then we extracted the relationship between c (from each group) and k and the mean radius of each group (calculated as the average of the lower and upper radius threshold of each group) and applied it to our simulation. We also performed a sensitivity analysis in which we investigated how the steady state solution is influenced by the vessel network structure through random or specific perturbations of the network properties to simulate relevant clinical cases. See more details in Appendix D, available in the online supplemental material.

2.10 Whole-Brain Blood Flow Simulation

In order to study the effect of the CoW in the regulation of blood pressure and flow, we connected all five compartments in the GBM dataset to a simplified CoW model to form a whole-brain artery network (called GBM-Wb) [36]. Note that in the GBM dataset, the LPCA communication artery is missing. The radius, length, c, k of the three incoming branches from the heart (i.e., left internal carotid artery (LICA)/right internal carotid artery (RICA)/vertebral artery (VA)) were slightly modeified such that the model produced reasonable pressures at the CoW region. We first generated a healthy reference subject by applying the radius versus graph level relationship obtained from BraVa dataset to the new GBM-Wb network. We then interpolated the radius of each branch for the time between healthy state (time step T_0) and 2013 (time step T_4) by assuming the radius of each branches varied linearly between the two time steps. In total, we have five equally spaced time steps T_0 through T_4 where T_1 , T_2 and T_3 are calculated using liner interpolation. For time step T_0 , we generated a ground truth solution by manually setting the flow by assuming that the blood flow split proportional to the crosssectional area of the child branches at each bifurcation. For the remaining four time steps, we solved the system for pressures and flows in order to answer the question of why the radius of arteries changed in the way we saw. For each of these time steps, we set the pressures of each terminating nodes as a boundary condition using the formula

$$P_0 - TP_{j,T_i} = \frac{(P_0 - TP_{j,T_0}) \cdot (V_{j,T_0} - V_{j,T_i})}{V_{j,T_0}}.$$
 (4)

Where $P_0=120$ mmHg is set as the root pressure at the heart, V_{j,T_i} is the total volume of the compartment that the jth terminating node belongs to, and TP_{j,T_i} is the pressure of the jth terminating point at time step T_i . We solved the system by minimizing the error related to a system of equations, which was composed of flow conservation equations at each bifurcation and H-W equations for each branch. The error in each flow conservation equations are

$$\sum_{i} Q_{in,i} - \sum_{j} Q_{out,j}.$$
 (5)

And the error in the H-W equations are

$$\Delta P_i - \frac{10.67 \cdot Q_i^k}{c_i^k \cdot d_i^{4.8704}} \cdot L_i. \tag{6}$$

The combined error, which is also the objective function of the minimization, is expressed as

Combined error =
$$\sum_{i} (\text{Flow error}_{i} \cdot 20000)^{2} + \sum_{j} (\text{H-W error}_{j} \cdot 500)^{2}.$$
 (7)

Weights are added to flow error and pressure error terms so that they are roughly on the similar magnitude. Since the objective function is nonconvex, we employed a global optimization solver using the basinhopping technique [37] to search for the global minimum. See more details in Appendix C, available in the online supplemental material.

2.11 Tumor and Edema Segmentation Procedure

Much efforts have been invested on automated tumor segmentation methods in recent years (e.g., Multimodal Brain Tumor Segmentation Challenge (BraTS)), however, since for this project we needed to analyze a single patient dataset, we manually segmented those images. To obtain tumor segmentation for each time point the following acquisitions protocols were used: 1) T1: T1-weighted axial orientation with 5 mm slice thickness; 2) T1c: T1-weighted gadolinium contrast enhanced with 1 mm isotropic resolution; 3) T2: T2-weighted axial orientation with 5 mm slice thickness; 4) Flair: T2-weighted FLAIR image with 1 mm isotropic resolution.

2.11.1 Preprocessing

All image volumes were co-registered via affine transformation to the MRA volume. In order to accomplish this and minimize registration errors, given that multiple surgeries occurred over the life of the patient, the registration process was as follows: 1) For each time point co-register T1, T2, and Flair modalities to the T1c image volume; 2) For the first time point with the MRA image register the T1c volume to the MRA volume; 3) For each consecutive time point register the T1c volume to the T1c volume of the time point preceding it; 4) Apply the transformations generated from the previous step to the T1, T2, and Flair modalities for each respective time point. These steps were performed using 3D Slicer's General Registration (BRAINS) and Transforms modules. Without this incremental registration significant errors occurred. The resulting registered volumes were than resampled with linear interpolation using a reference volume with 1 mm resolution and orthogonal image axes. The image volumes were then bias corrected using N4ITK bias correction [38] and normalized using linear normalization.

2.11.2 Segmentation

Segmentation was achieved using tools in 3D Slicer's segment editor module. 1) Edema was segmented primarily from FLAIR images. A threshold value was determined visually for each region and then a spherical brush was used to paint over the region segmenting voxels above the given threshold. In most cases the segmentation of the previous time point was used as a starting place and segmentation was added and removed as necessary. The segmentation was filtered using a median filter of size 3 and then smaller details were re-segmented. 2) Tumor was primally segmented from visualization of intensity changes over time in T1c verified by radiologist's notes on tumor progression, location, and size. Radiologist notes and visual progression indicated which areas were likely tumor, then these areas were painted with and without intensity thresholding to capture enhancing and nonenhancing tumor. Previous time point's segmentation was usually used as a starting point to ensure consistency. FLAIR images were also used to help distinguish between vessels in certain cases. T1 images were cross-referenced to distinguish against hemorrhaging. The resulting segmentation was filtered using a median filter of size 3 and then smaller details were re-segmented.

3 RESULT

The main contribution of our work is to provide an automated, personalized, system-level approach to analyzing how changes in the brain arterial network of a GBM patient could result in blood flow behavior that is advantageous to development of the cancer over time, using common clinical patient data. We showed that in individuals with GBM, arterial radius changes are driven by two 'forces', spatiotemporal tumor-related constraints, and a brain compensatory mechanism that tries to overcome arterial changes by restoring brain homeostasis. Our analysis includes the following steps: First, we develop a tool to measure and observe the changes in properties of an arterial network due to GBM. Second, we provide a detailed comparison with healthy arterial networks, to appreciate the contribution of differences in resolution in multiple datasets. This step can also serve as an independent resource. Third, we present a case study of GBM, analyzed by the current clinical approach. Fourth, we provide a system-level analysis of the GBM arterial network structure. Lastly, after measuring the patient's structural changes over time, we simulate the mean blood flow dynamics, to assess evolution of the arterial network due to the tumor and brain function.

Potential future consequences of our work could infer the disease stage given the adaptation stage of the arterial network, separate between different responders, select treatments with minimum impact on the arteries, integrate genomic data with the adaptive arterial network of a patient, to advance GBM predictions.

3.1 Tracking the Topological Properties of the 150-250 μ m High-Resolution Arterial Network

To study the expected arterial network (i.e., control, normal subset), we analyzed the most detailed healthy human subject's arterial network available to date. Recently, Speck and colleagues [7], [8] imaged a single healthy brain arterial network at very high resolution (250 μm T1-weighted whole brain anatomical data [8], and 150 μm limited-area of brain MRA [7]). We created an integrated image from the two images. The segmentation pipeline of the merged dataset using our approach includes several steps, which are described in Section 2, Fig. 2 and Video 1.

The combined network has a total length of about 8,676 mm, with a maximum of 20 bifurcation nodes per path (i.e., graph level). A path distance can be up to 282 mm, with a wide range (3 orders of magnitudes) of bifurcating and terminating branch lengths (see Fig. 3a). A negative relationship between radius and graph level is apparent (Fig. 3b). Graph topological properties also include spatial elements per node or branch, such as node amplitude and branch curvature. A detailed summary can be found in Table S3 and Fig. S1, available in the online supplemental material. Analysis of left and right hemispheres shows that they are far from being locally identical. Although, both sides peak at different graph levels, include slightly dissimilar radius distributions, and different tree structures, yet these differences are not statistically significant at the population level. It would be difficult to compare branches one-to-one in the left and right hemispheres of a healthy individual, and obviously when one is damaged. Even for the main arteries of the Circle of Willis, anatomical variations are common in healthy subjects [39]. It is important to note that not every artery's abnormality may cause or contribute to the development of a disease. Thus, once comparing cases, we focused on major trends and relationships between the variables and properties (see Appendix A), available in the online supplemental material. This arterial network segmentation and its structural analysis categorization can serve as an *atlas*, due to its unique high-resolution image information.

3.2 Variations in Structural Properties of Arterial Networks When Determined From a Higher Resolution Image

To assess the information gained concerning structural network properties from a higher resolution image, we compared the Speck et~al. integrated network (150/250 μm) with the BraVa networks (600 μm MRAs) [9], [40], which analyzed the brain artery properties of 61 healthy subjects. Using the Speck highest resolution dataset, we calculated the arterial network properties and investigated the difference between the Speck high resolution graph and one representative example of the healthy subjects from BraVa dataset that was chosen randomly. We also examined the trends and relationships between the variables with the mean behavior of BraVa population (Table S3, Fig. 3, Fig. S2), available in the online supplemental material.

While the Speck graph is quite detailed, it is interesting to find that the main distribution results agree with the BraVa estimations, while the numbers of nodes/edges are different, and include a wider variations per graph's property. To compare the bifurcating and terminating nodes within each dataset, the BraVa dataset indicated that the terminating branches on average are 73 percent longer, and are 28 percent more tortuous (i.e., twisted branches) than bifurcating branches. We found that terminating branches are more tortuous (p < 0.001 using Student's t testMann-Whitney U-test) than bifurcating branches. However, our analysis of the high-resolution network shows that there is no significant difference in length between bifurcating and terminating branches (p = 0.15p = 0.29 using Student's t testMann-Whitney U-test). This difference could be due to the resolution limit of the BraVa data, thus mistakenly considering bifurcating branches as terminating branches. This difference could be because some terminating branches in the BraVa dataset might be a portion of bifurcating branches in the higher resolution image. Either, the image cannot capture the additional information, or for other reasons such as image artifact, and disconnected branches. Moreover, the BraVa dataset showed that length and tortuosity of the bifurcating branches increased with path distance from the CoW, which we did not observe in the Speck dataset. Both datasets showed no left or right hemisphere dominance concerning local or remote branching angles and they did not vary to any great degree throughout the network.

3.3 A Case Study of LGG to GBM Evolution Based on a Patient's Clinical Data

We next analyzed the data of one GBM patient with time series modalities of MRI brain perfusion (sMRI 1 mm) from 2010 to 2016, and a single MRA (400 μ m) performed in 2013. This patient's tumor began as an LGG (initially identified on

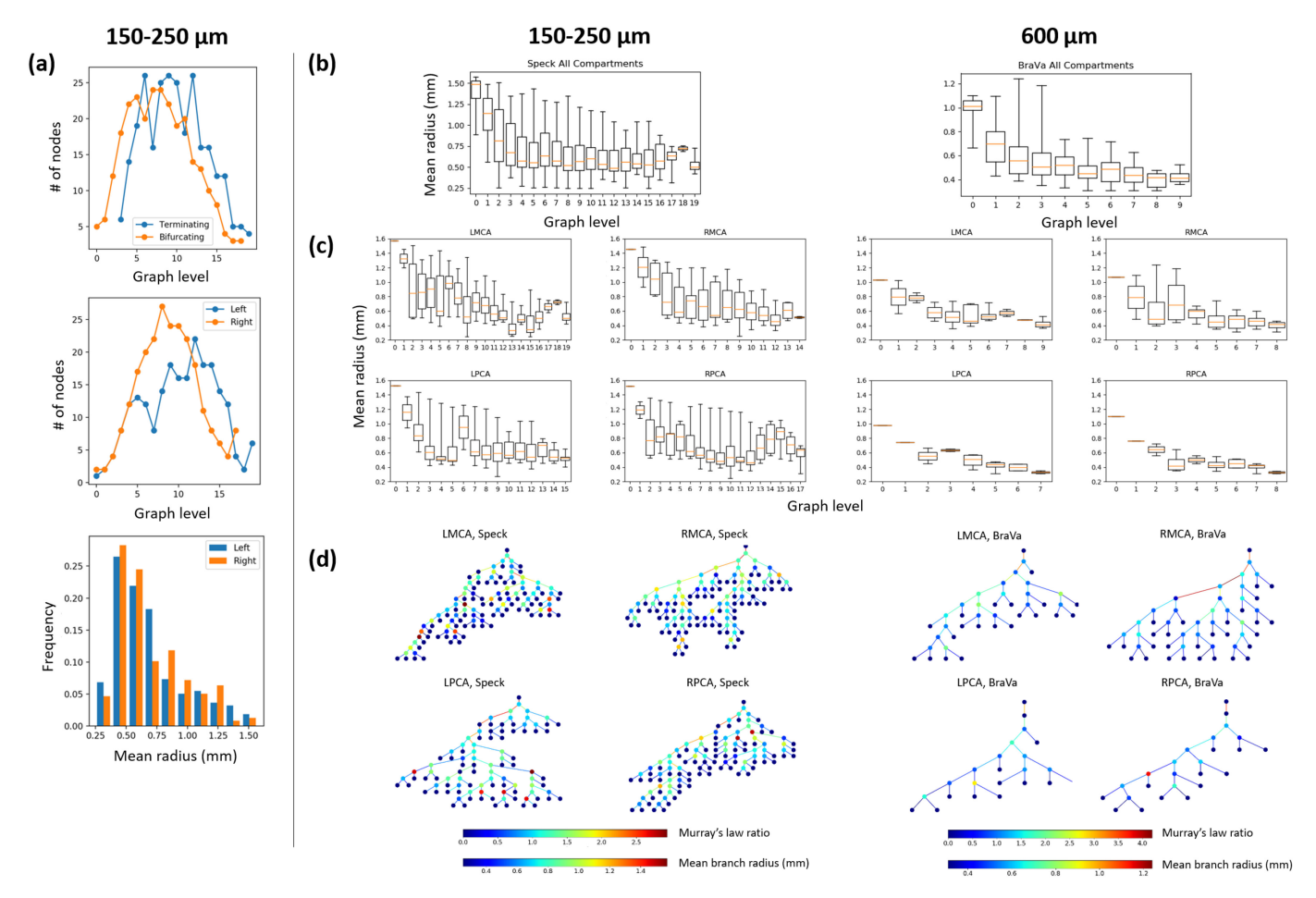


Fig. 3. Network properties of the Speck and BraVa dataset. (a) Number of terminating/bifurcating nodes versus graph level, number of nodes for left and right hemisphere versus graph level, mean branch radius distribution between left and right hemisphere. The latter two show that there are no hemispheric dominance between left and right hemisphere. (b) The mean branch radius decreases with increasing graph level in a similar way for both Speck and BraVa dataset. (c) LMCA/RMCA/LPCA/RPCA in both the Speck and BraVa dataset exhibits roughly similar branch radius versus graph level relationship. (d) The graph structure (LMCA/RMCA and LPCA/RPCA) are similar for Speck and BraVa dataset. Network topological properties of healthy individuals. Data presented here are from the Speck dataset, and from one subject randomly chosen from the BraVa dataset. (a) Comparison between number of terminating/bifurcating nodes as a function of graph level, and comparison of left and right hemispheres of the high-resolution arterial network (Speck dataset). The latter two show that there is no hemispheric dominance of either the left or right hemisphere. (b) The mean branch radius decreases with increasing graph level in a similar way for both Speck and BraVa subject datasets. (c) Compartments (LMCA/RMCA/LPCA/RPCA) in both datasets exhibit similar branch radius versus graph level relationships. (d) The main graph structures (LMCA/RMCA and LPCA/RPCA) of the Speck and BraVa subject datasets are similar. The Speck graph includes many more nodes and is higher in graph level. The color of each node represents cubic Murray's law ratio, whereas the color of the edges represents mean branch radius.

2008) that later transformed into GBM (in 2012). We received a clinical assessment from a trained diagnostic neuroradiologist who assessed the disease progression longitudinally based on the current clinical approach and the patient data. The patient's clinical data were further reviewed and interpreted by another trained neuroradiologist who was blinded to the purpose of this study (see Appendix B), available in the online supplemental material. Independently, we ran our pipeline and analyzed the patient's arterial network, and compared the results of the two assessments. Then we evaluated how accurate the assessments were at predicting disease progression, based on the sMRI after 2013.

3.4 Current Neuroradiological Assessment Focuses on Local Changes

Neuroradiologists mainly commented on the transformation of LGG to GBM, spatiotemporal progression pattern, and brain MRA assessment. In brief, there were two transformations from LGG to GBM, the first occurred in May 2012, and

second after September 2014. Two surgical intervention were performed with resection of areas of GBM lesions after 2013. The lesion continued to increase in size leading to the patient's death in October 2016. An abnormal brain MRA (semi full brain size) was reported in May 2013 following surgical excision of areas of abnormally enhancing tissue in the left frontal lobe. There was a 4 mm short segmentbranch of high-grade stenosis of the M1 segmentbranch of the left middle cerebral artery. A focal point of irregularity was seen in the M1 segmentbranch of the right middle cerebral artery as well. There was hypoplasia of the left anterior cerebral artery and asymmetry of the left carotid arteries. Distal branches of the middle cerebral arteries and anterior cerebral arteries and peri-callosal arteries were patent (enhanced). The etiology of these findings was unclear, but the images suggested a developmental vascular anomaly versus an acquired injury from prior radiation treatment, especially as radiation-induced vasculopathy could be seen on subsequent imaging dated April 2014. No visualized collateral

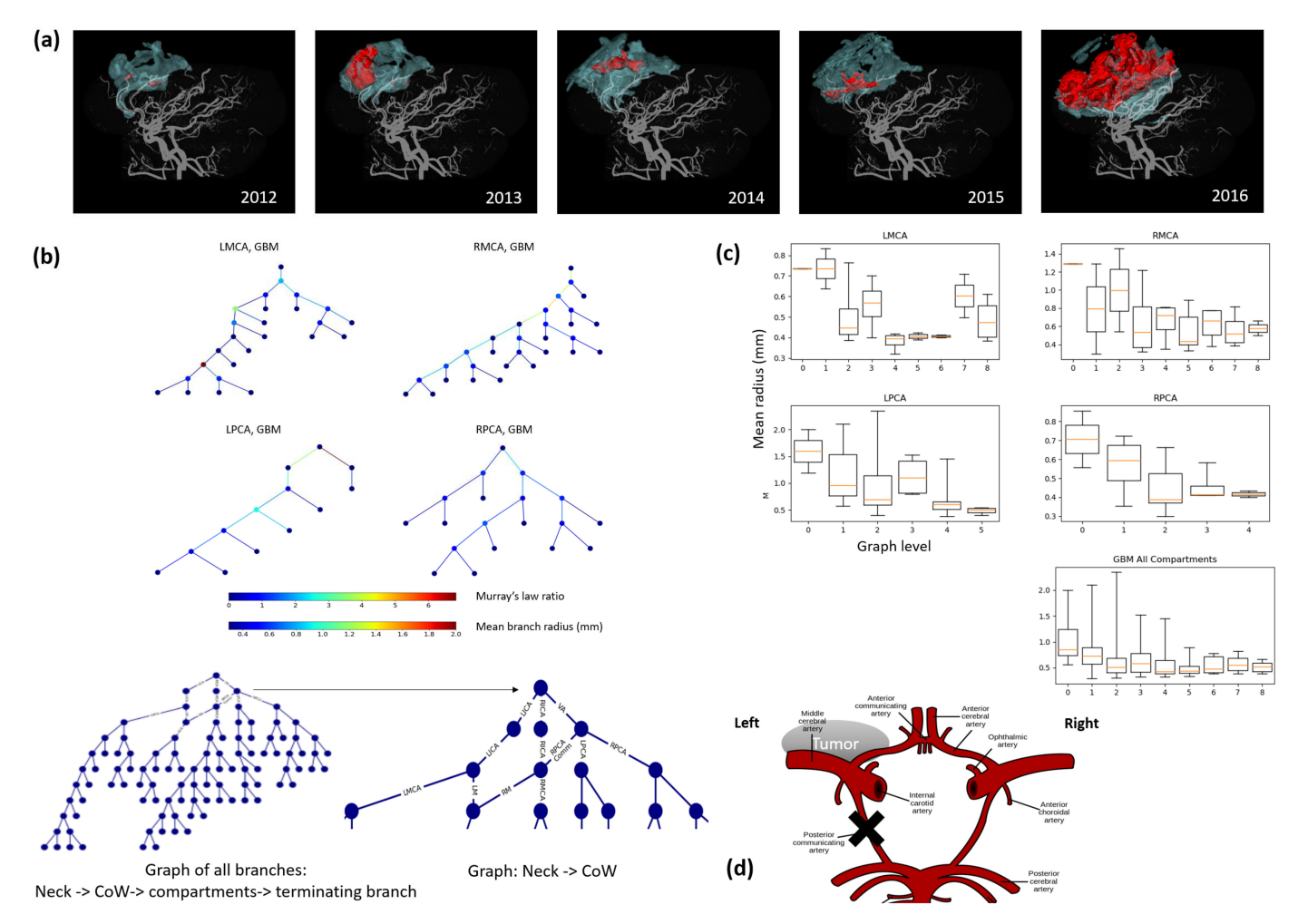


Fig. 4. GBM study case. (a) A sequence of T1 image from the GBM patient taken from 2012 to 2016 showing the progression of tumor growth. (b) The structure of the LMCA/RMCA and LPCA/RPCA compartment of the GBM subject. Note that although its resolution (400 μ m) is better than the BraVa dataset (600 μm), we see significantly less arteries. (c) Comparison of the mean branch radius versus graph level for different compartments in GBM dataset shows that the tumor in the GBM patient causes the radius of the arteries in LMCA/RPCA to decrease and that in RMCA/LPCA to increase. (d) A diagram showing main arteries around the Circle of Willis (the GBM patient is missing the left posterior communicating artery). (Source: Wikipedia)GBM patient's arterial network. (a) A sequence of T1 images from a GBM patient taken from 2012 to 2016 showing the progression of tumor growth and surgical area. The segmented tumor is colored in red, the segmented edema is colored in light blue and the arteries in gray, shown using the maximum intensity projection (MIP). The tumor originally started as LGG in the left anterior area, later penetrated as GBM to the right anterior lobes, and from 2015 spread to the left posterior area. We focus on GBM progression and arterial changes during those time periods. (b) The graph structures of the LMCA and RMCA compartments based on a GBM patient's MRA taken in 2013. Note, although the MRA resolution (400 μm) is higher than the healthy subjects in the BraVa dataset (600 μm), we see significantly fewer arteries due to the treatments and disease progression. The color of each node represents cubic Murray's law ratio, whereas the color of the edges represents mean branch radius. We also include the complete graph that includes all branches from the neck to CoW to compartments to terminating branches. (c) Comparison of the mean branch radius versus graph level for different compartments in the GBM dataset shows that the tumor causes the radius of the arteries in LMCA & RPCA to decrease and the radius in RMCA & LPCA to increase. MCA branches mainly cover the physical space of the anterior lobes, while PCA can cover the posterior area of the brain. (d) A diagram showing the main arteries around the Circle of Willis, where the GBM patient is missing the left posterior communicating artery (Image illustration source: Wikipedia and [41]).

vascularization was seen (see Appendix B), available in the online supplemental material.

3.5 Analysis of the Entire Arterial Network Complements Information to Assess Disease Progression

Our topological analysis included two steps. First, we examined *all* local changes, beyond the main CoW arteries (as was made by the common neuroradiological approach). Moreover, we studied their global effects on the network structure. Our analysis provides all radius distributions of each network's compartment, so a comparison with healthy cases can be performed. In addition, to emphasis the connection

between tumor growth pattern to arterial network, we provide a unique video. Tumor progression can be visualized over time, compared to the limited MRA area that was taken in 2013 (see Video 2, and Section 2). By providing our segmentation of the tumor and edema over time, and including the reference arterial network based on a single MRA, the pattern of GBM progression can be observed.

The tumor is located between the ACA and LMCA areas. Over time it spreads mainly through the LMCA, where some cells invaded to the RMCA area (Fig. 4a). Based on our structural network analysis, we found that there was a global change throughout all graph levels. To be able to compare the GBM case with a healthy subject with close image resolution,

we randomly chose one representative subject from the BraVa dataset. This showed a negative relationship between a mean radius at the graph level that began at 1 mm. However, the GBM relationship began at the first graph level, either greater than or less than a 1 mm radius. We found that the reduced branch radius, mentioned in the neuroradiologist's assessment, occurred at the first two graph levels (e.g., first branch in ACA, and M1 in MCA). However, there were many significant changes in the mean radius at higher graph levels, specifically levels 4-6, that were imperceptible using the current neuroradiological approach (Fig. 4c). The branch radii in the left cerebral arteries (LMCAs) were significantly smaller than those in the right cerebral arteries (RMCAs), with distorted distribution. It is interesting to point out that on graph level 2, where the LMCA had a reduced mean radius, the RMCA had an increased mean radius, which clearly demonstrate compensation between the two left-right compartments. Both LMCAs and RMCAs, on graph level 2, showed high variation in radius size. While the compensation between left and right hemispheres with some fluctuations (around 1 mm in initial mean radius on graph level 1) may be reasonable, the more striking structural network changes are the adaptations on the posterior side versus the anterior side, where the tumor is located. Examining the LPCA, we found that the mean radius length was twice that of the LMCA. This increase occurred throughout all graph levels in the LPCA, beginning at 2 mm.

Moreover, we found that the left posterior communicating artery branch was absent, which was not noticed in the clinical exam. Since there was surgery in 2013, we examined a previous T1 image of 2010, and determined that most likely this was a developmental defect, and not due to the surgery. It is important to note that the extraction of a full arterial network from T1 images after treatments was not possible; only parts of the network could be recovered. However, an MRA can provide the entire patient's network. Yet, by comparing CoW branches in 2010 versus 2013, we found a general decrease in all radii, with greater changes occurring on the left side than on the right side. We further examined the changes of the main CoW arteries over time until 2016 based on T1 images, and found that all arteries were dynamically changing, and the left M1 in the MCA branch continued to significantly decrease in radius over time. Lastly, we asked, regardless of the disease, could the absence of the left posterior communicating artery branch simply be the cause of the LPCA compensation? To answer this question, we examined the results of a study by Krabbe-Hartkamp et al. [39] about morphological variation of CoW arteries in healthy subjects. Subjects with no posterior communicating artery branch (left or right), demonstrated no changes in other CoW arteries, proving that the observed compensation is the results of the GBM disease progression, and not the intrinsic developmental structure.

3.6 Mean Blood Flow Behavior Reveals Parts of GBM Evolution

After identifying the structural changes in the patient's arterial network on a system scale, we asked how those changes would impact brain hemodynamics. Furthermore, we were

interested to answer why the GBM patient had such spatiotemporal changes in the arterial network, and how they could have been evolved from its normal or earlier phase to its advanced MRA state in 2013. To address these challenging questions concerning adaptive hemodynamics behavior, we developed a mathematical model. Given the lack of detailed brain blood flow data, especially information on brain pressure in terminating nodes, from a systematic clinical screening, we assessed mainly the steadystate solution. From a simplified math model inspired by the Hazen-Williams (H-W) equation, we applied the model to the detailed network extracted from the patient's image (see detailed description of the model and all steps and results in Appendix C, Section 2, Fig. S11), available in the online supplemental material. Note, we do not directly include the tumor consumption or its occupying space, but rather examine the brain arteries as a sensor to the perturbed brain behavior (Appendix E), available in the online supplemental material.

Given the lack of time series MRAs, we first generated a healthy reference network by applying the radius versus graph level relationship obtained from the BraVa dataset to the GBM patient's network structure. At each bifurcation, we assumed the flow split in a way that is proportional to the cross-sectional area of its 'child branches'. We then interpolated the radius of each branch for the time between healthy state and GBM state in 2013, by assuming that the radius of each branches varied linearly between the two time steps. Based on our simulations, there are several important results that add information to our structural network analysis (Fig. 5a). Mainly, the results reveal an interplay between the tumor and the brain compensatory mechanism. First, the total flow to the brain decreases over time, as the brain gets less blood flow to compensate for the high tumor demands. While the actual flow on the left side decreases, the proportion going to the LMCA increases. Specifically, LMCA and RPCA increases. RMCA decreases and the rest are quite stable. Interestingly, even though the LMCA and RPCA compartments do not share the same trend in terms of radius change, their blood flow increases. From the compartment-based distributions of terminating pressure nodes, an asymmetrical pattern emerges to offset flow to the left (LMCA+LPCA) and right (RMCA+RPCA) sides, and to offset upper (MCA) and lower (PCA) areas (Fig. 5b). LMCA and RPCA decrease, while RMCA and LPCA increase. Altogether, the tumor affected the arterial network in three ways. Higher blood demand on one side was created, changing the radii of arteries, and by regulating the neighboring terminating pressure nodes. Since the tumor was located mainly on the left side, next to the LMCA and LACA, the neighboring terminating pressure nodes were changed, thus creating a higher pressure drop. In return, the blood flow changes and compensatory mechanism adjusted the entire arterial structure to maintain the homeostasis, as much as possible, at a given time point. The CoW compensatory mechanism led to a non-linear relationship between the radius changes, terminating pressure and blood flow patterns. Moreover, at time points T2-T3 (reflect the year of 2012), blood flow values at PCA showed a fluctuating pattern, even though the radius of each branch varied linearly between the two time points.

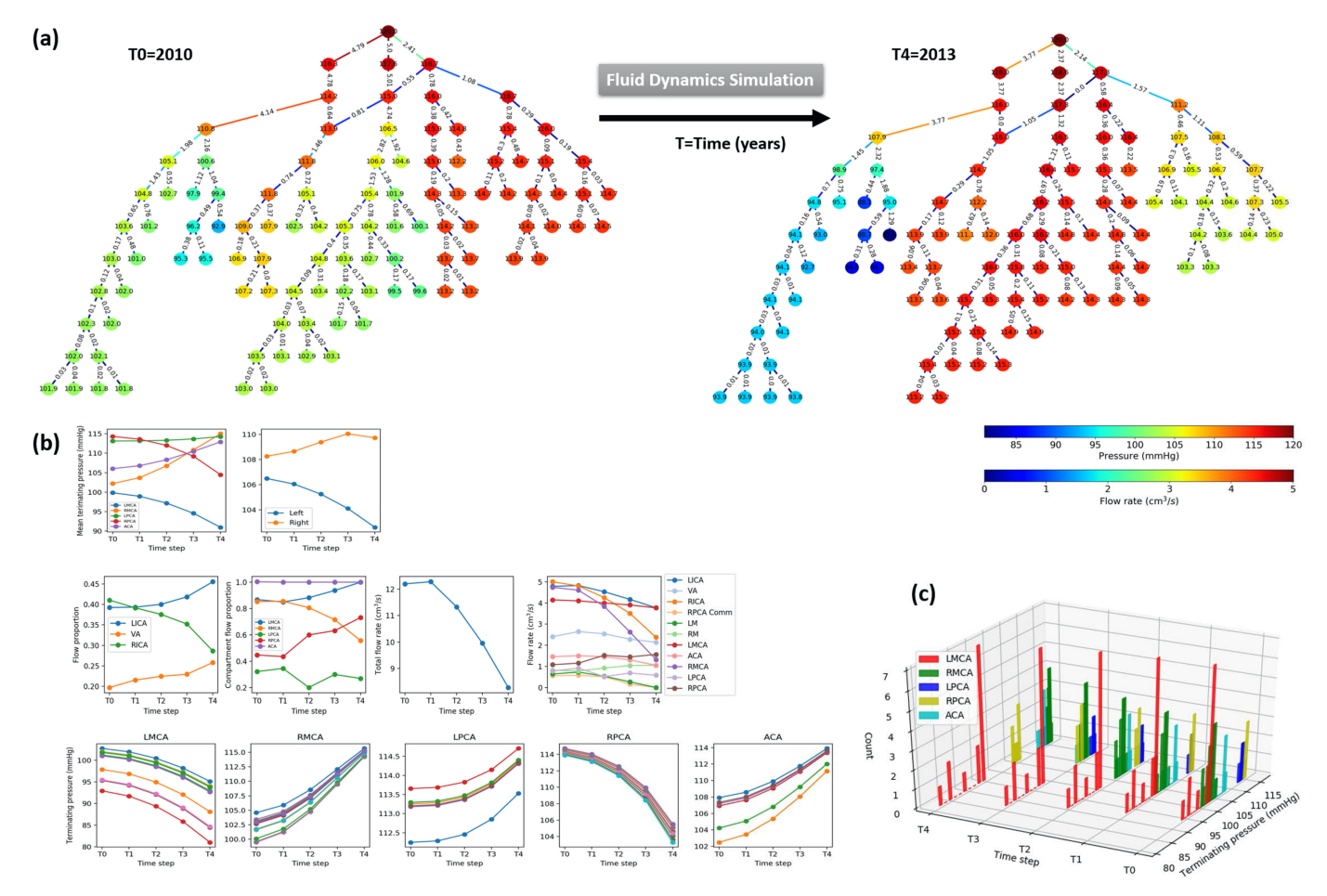


Fig. 5. (a) Simulated pressure and velocity of one compartment between time step T_0 and T_4 . Node values/colors represent the pressure and edge values/colors represent flow rate. (b) Various flow properties among the five time steps. (c) Terminating pressure distribution among the five time steps. Mean blood flow dynamics in evolving GBM. (a) Graph plot of the GBM network of pressures and flow rates at two different time points ($T_0 = 2010$ till $T_4 = 2013$). The color and the value of each node refer to the pressure at that node and the color and the value on each edge refer to the flow rate in that branch. This plot shows that the changes are not just near the tumor, but global due to brain function. (b) Bottom: Change of terminating pressures with respect to the five time points (each color in the subplot refers to a terminating node). Middle: Flow proportions and flow rates with respect to the five time points. Top: Mean terminating pressures per compartment or hemisphere. Their value changes are significant during GBM progression ($T_0 = 2010$ till $T_4 = 2013$). (c) 3D histogram of the terminating pressures per compartment and five time points ($T_0 = 2010$ till $T_4 = 2013$).

4 Conclusion

Glioblastoma multiforme is the most lethal adult primary brain cancer and remains incurable despite decades of research [42]. There is substantial evidence showing that GBM development is not solely an intrinsic cellular process driven by epigenetic/genetic perturbations, but is also heavily dependent on the different microenvironments that form the brain's topology. Brain anatomy, including the brain parenchyma, pre-existing blood vessel network, white matter tracts, and the subarachnoid space below the meningeal covering of the brain, all play important roles in GBM aggressiveness and its resistance to treatments [43]. The brain environment is far from homogeneous, and has three GBM related fundamental spatial environments: the brain parenchyma (BP), the perivascular space (PS), and the white matter tracts (WM). These parts are rich with spatial brain and tumor microenvironment stimuli, including mitogens (EGF and PDGF), other key pathway drivers (TIMP and WNT Canonical, impacting TGFB and WNT signaling), and various attributes of the internal and external environment (DNA Damage, Oxygen, Bradykinin, Ephrin B1/B2, Stiff ECM Components, Hyaluronan). Through a cellular machinery, GBM cells react to those stimuli by switching between the different phenotypes of Go, Grow, Dormant, and Apoptosis [43], [44].

For instance, along white matter tracts, a range of axonal guidance molecules are known to direct movement of neural precursor cells during development. GBM tumor cells co-opt some of these mechanisms, including experimentally established pathways leading from Ephrin B1 and B2 to direct motility, via activation of the EphB2 receptor, FAK, and RHOA [45]. Such information and the well known Scherers Secondary Structures of GBM, encourage researchers to mathematically model tumor growth using MRI and DTI [46] and others to offer patient prognosis methods based on the intersection between location of brain tumor with white matter tracts [47]. However, the experimental research of motility along the WM tracts is not as detailed, and not advanced in developing targeted drugs, as other motility pathways. In addition, tracking tumor growth using MRI + DTI has its own limitations. In a study conducted by Morteza Esmaeili et al. [48], it was shown that the alignment between

tumor growth and DTI has low correlations, which suggests that there are other significant mechanisms involved. The next question is what are those other measurements and how exactly can one use them to address the GBM progression problem, using patient data?

This scientific exploration led us to the current study, in which we suggest integrating another component, the arterial network using patient MRA. Apart from the obvious dependency of a tumor on the arterial network due to its high consumption of nutrients, GBM cells also follow the perivascular space. In the perivascular space, extracellular bradykinin acts through a G-protein-coupled receptor to increase intracellular Ca²⁺, leading to Ca²⁺-dependent efflux of Cl⁻ and K⁺ through ion channels. This leads to water loss from the cell by osmosis and consequent volume reduction, which facilitates movement amidst astrocytic end feet and other local barriers in the perivascular space [43]. While this mechanism of motility is well known to be experimentally proven, no imaging technique has been offered to track those motile cells based on arterial network information, nor their impact on the disease and patient brain, in a systematic way.

In this work, we provide, for the first time, a new computational technology that is distinct from approaches that have been used for GBM. We offer to integrate a key layer of the brain's components, the arterial network, and study its adaptation during the evolution of GBM. The arteries are an essential part of GBM development, not just as a way to deliver drugs or nutrients, but also as a physical pathway for GBM motile cells. This process is driven by the network location, structure, and fluid dynamics of blood. Therapeutic treatments do change the arterial network, in many ways. Our work shows that the process of tumor development is regulated by the brain's compensatory processes. One is left to wonder if such a communication sub-system exists, could we use it in other ways? For instance, 1) If tumor cells cannot be detected by MRIs, could we use the adaptation stage of the arteries to infer the disease stage? 2) Could we use the arterial network properties to separate between different responders? 3) Should a particular drug be used, given changes it may induce in the arterial network? 4) Could the integration of genomic data and adaptive arteries advance our predictions?

The current, most advanced clinical approach to treating GBM does not involve a full brain arterial network analysis, unless there is a concern and thus a very limited local examination will be conducted. Out of a NIH dataset of 400 GBM patients, with about 3800 clinical follow-ups, a semi-full brain MRA scan was performed for only a single patient, throughout the entire treatment period. We propose to add to the routine clinical assessment not only a time series MRI brain-perfusion (at least 1 mm in resolution), but also time series brain MRA scans (at least 400 μ m), to allow the development of a more comprehensive personalized computational study (including deep learning of complex dynamical systems) of the arteries and their compensation due to the disease progression. Our automated method could easily be applied to large cohort of patients, perform a large statistical analysis to reliably identify markers of glioblastoma.

Neuroimaging plays an important and evolving role in the diagnosis, treatment planning (surgical and medical interventions), and post-therapy assessment of brain disease [49],

[50]. However, clinicians and surgeons are faced with significant challenges concerning the accuracy of diagnosis and treatment management, as most are based on a series of clinical imagesstandard of care imaging data, which may sometimes be misleading. For example, a suspicious lesion may lead to uncertainty concerning post-treatment effects, and may be due to pseudoprogression, or tumor recurrence. Similar issues arise with immunotherapy response [51], [52]. It is challenging to determine whether a patient has responded well to the treatment or if an image has been over-enhanced for other reasonsenhancement that is not driven by underlying disease. An even more problematic problem is the inverse, in which tumor cells cannot be identified by MRIs. How can we predict, with reasonable accuracy, the spatial migration distribution of glioblastoma cells when enhancing lesions cannot be detected by MRIscontrast to noise ratio between the enhanced lesion and healthy brain is not high enough? While the first problem of over enhancementnondisease driven enhancement could be resolved in the future by advanced deep learning methods, the second problem of non-detected signals needs a better re-thinking of the approach, concerning measurements and data analysis. For such provoking cases, it would be wiser to explore and include complementary indirect system-level approaches to draw conclusions about the disease. We offer to track the adaptation and compensation processes of patients' brain arterial network to infer properties of glioblastoma.

ACKNOWLEDGMENTS

OL would like to thank Dr. Michael M. Gottesman (Laboratory of Cell Biology, CCR, NCI, NIH) and Dr. Tom Misteli (Laboratory of Receptor Biology and Gene Expression, CCR, NCI, NIH) for their critical comments and support. The authors would also like to thank Mr. George Leiman (LCB, NCI, NIH) for editorial assistance, and Andrea Beri from NIH/CC/BTRIS program for providing the data. This work was supported by the Intramural Research Program of the NIH, National Cancer Institute, Center for Cancer Research. All authors wrote, read and approved the manuscript.

REFERENCES

- [1] A. Armento, J. Ehlers, S. Schötterl, and U. Naumann, "Molecular mechanisms of glioma cell motility, " in, *Glioblastoma [Internet]*. Brisbane, Australia: Codon Publications, 2017.
- [2] M. D. Sweeney, K. Kisler, A. Montagne, A. W. Toga, and B. V. Zlokovic, "The role of brain vasculature in neurodegenerative disorders," *Nat. Neurosci.*, vol. 21, no. 10, pp. 1318–1331, 2018.
- [3] L. Edvinsson, E. T. MacKenzie, and J. McCulloch, in Cerebral Blood Flow and Metabolism, New York: Raven Press, vol. 1185, 1993.
- [4] B. K. Lal et al., "Asymptomatic carotid stenosis is associated with cognitive impairment," J. Vascular Surgery, vol. 66, no. 4, pp. 1083–1092, 2017.
- [5] A. Goriely et al., "Mechanics of the brain: Perspectives, challenges, and opportunities," Biomechanics Model. Mechanobiol., vol. 14, no. 5, pp. 931–965, 2015.
- [6] X. Li et al., "Retrospective study of hemodynamic changes before and after carotid stenosis formation by vessel surface repairing," Sci. Reports, vol. 8, no. 1, 2018, Art. no. 5493.
- [7] H. Mattern et al., "Prospective motion correction enables highest resolution time-of-flight angiography at 7T," Magn. Reson. Medicine, vol. 80, no. 1, pp. 248–258, 2018.
- [8] F. Lüsebrink, A. Ściarra, H. Mattern, R. Yakupov, and O. Speck, "T1-weighted in vivo human whole brain MRI dataset with an ultrahigh isotropic resolution of 250 μm," Sci. Data, vol. 4, 2017, Art. no. 170032.

- S. N. Wright et al., "Digital reconstruction and morphometric analysis of human brain arterial vasculature from magnetic resonance angiography," Neuroimage, vol. 82, pp. 170-181, 2013.
- [10] P. J. Blanco, S. M. Watanabe, M. A. R. Passos, P. A. Lemos, and R. A. Feijóo, "An anatomically detailed arterial network model for one-dimensional computational hemodynamics," IEEE Trans. Biomed. Eng., vol. 62, no. 2, pp. 736-753, Feb. 2015.
- M. Jenkinson, C. F. Beckmann, T. E. Behrens, M. W. Woolrich, and
- S. M. Smith, "FSL," Neuroimage, vol. 62, no. 2, pp. 782–790, 2012.

 [12] D. N. Greve and B. Fischl, "Accurate and robust brain image alignment using boundary-based registration," *Neuroimage*, vol. 48, no. 1, pp. 63–72, 2009.
- [13] M. Jenkinson, P. Bannister, M. Brady, and S. Smith, "Improved optimization for the robust and accurate linear registration and motion correction of brain images," Neuroimage, vol. 17, no. 2, pp. 825-841, 2002.
- [14] M. Jenkinson and S. Smith, "A global optimisation method for robust affine registration of brain images," Med. Image Anal., vol. 5, no. 2, pp. 143-156, 2001.
- [15] A. F. Frangi, W. J. Niessen, K. L. Vincken, and M. A. Viergever, "Multiscale vessel enhancement filtering," in Proc. Int. Conf. Med. Image Comput. Comput.-Assisted Intervention, 1998, pp. 130-137.
- A. Fedorov et al., "3D slicer as an image computing platform for the quantitative imaging network," Magn. Reson. Imag., vol. 30, no. 9, pp. 1323-1341, 2012.
- [17] T. E. Oliphant, "Python for scientific computing," Comput. Sci. Eng., vol. 9, pp. 10-20, 2007.
- [18] J.-L. Rose, T. Grenier, C. Revol-Muller, and C. Odet, "Unifying variational approach and region growing segmentation," in Proc. 18th Eur. Signal Process. Conf., 2010, pp. 1781–1785. [19] T. Jerman, F. Pernuš, B. Likar, and Ž. Špiclin, "Beyond frangi: An
- improved multiscale vesselness filter," in Proc. Med. Imag. Image Process., 2015, Art. no. 94132A.
- [20] S. Moccia, E. De Momi, S. El Hadji, and L. S. Mattos, "Blood vessel segmentation algorithms review of methods, datasets and evaluation metrics," Comput. Methods Programs Biomed., vol. 158, pp. 71-91, 2018.
- P. A. Govyadinov, T. Womack, J. L. Eriksen, G. Chen, and [21] D. Mayerich, "Robust tracing and visualization of heterogeneous microvascular networks," IEEE Trans. Vis. Comput. Graphics, vol. 25, no. 4, pp. 1760–1773, Apr. 2019.
- [22] A. Tabb and H. Medeiros, "Fast and robust curve skeletonization for real-world elongated objects," in Proc. IEEE Winter Conf. Appl. Comput. Vis., 2018, pp. 1935-1943.
- T. G. Pock, "Robust Segmentation of Tubular Structures in 3D Volume Data," Master Thesis, University of Graz, 2004. [Online]. Available: https://pdfs.semanticscholar.org/66f3/0f806cb8dfbe fac9caeda9e58ebd86c88c46.pdf
- [24] G. S. Kassab, C. A. Rider, N. J. Tang, and Y.-C. Fung, "Morphometry of pig coronary arterial trees," Amer. J. Physiol. Heart Circulatory Physiol., vol. 265, no. 1, pp. H350-H365, 1993.
- [25] D. Turcotte, J. Pelletier, and W. Newman, "Networks with side branching in biology," J. Theor. Biol., vol. 193, no. 4, pp. 577–592, 1998.
- J. Wang, G. Chen, M. Li, and Y. Pan, "Integration of breast cancer gene signatures based on graph centrality," *BMC Syst. Biol.*, vol. 5, no. 3, 2011, Art. no. S10.
- [27] A. Özgür, T. Vu, G. Erkan, and D. R. Radev, "Identifying gene-disease associations using centrality on a literature mined gene-interaction network," Bioinformatics, vol. 24, no. 13, pp. i277-i285, 2008.
- [28] S. Lorthois, F. Lauwers, and F. Cassot, "Tortuosity and other vessel attributes for arterioles and venules of the human cerebral cortex," Microvascular Res., vol. 91, pp. 99-109, 2014.
- [29] B. J. Kim et al., "Vascular tortuosity may be associated with cervical artery dissection," Stroke, vol. 47, no. 10, pp. 2548–2552, 2016.
- J.-M. Chang et al., "Autism risk classification using placental chorionic surface vascular network features," BMC Med. Informat. Decis. Making, vol. 17, no. 1, 2017, Art. no. 162.
- [31] M. Rempfler, B. Andres, and B. H. Menze, "Uncertainty estimation in vascular networks," in Proc. Int. Workshop Graphs Biomed. Image Anal. Comput. Anatomy Imag. Genetics, 2017, pp. 42-52.
- [32] H. Bogunovic et al., "Geometric modeling and characterization of the circle of willis," Ph.D. dissertation, Dept. Inform. Commun. Tech., Universitat Pompeu Fabra, Barcelona, Spain, 2012. [Online]. Available: http://www.cistib.org/afrangi/pdf/thesis/hbogunovic.pdf

- [33] R. Scorcioni, S. Polavaram, and G. A. Ascoli, "L-measure: A webaccessible tool for the analysis, comparison and search of digital reconstructions of neuronal morphologies," Nat. Protocols, vol. 3, no. 5, 2008, Art. no. 866.
- [34] Y. Liu and G. S. Kassab, "Vascular metabolic dissipation in murray's law," Amer. J. Physiol.-Heart Circulatory Physiol., vol. 292, no. 3, pp. H1336-H1339, 2007.
- P. R. Painter, P. Edén, and H.-U. Bengtsson, "Pulsatile blood flow, shear force, energy dissipation and murray's law," Theor. Biol. Med. Modelling, vol. 3, no. 1, 2006, Art. no. 31.
- [36] L. Zarrinkoob, K. Ambarki, A. Wåhlin, R. Birgander, A. Eklund, and J. Malm, "Blood flow distribution in cerebral arteries," J. Cerebral Blood Flow Metabolism, vol. 35, no. 4, pp. 648-654, 2015.
- D. J. Wales and J. P. Doye, "Global optimization by basin-hopping and the lowest energy structures of lennard-jones clusters containing up to 110 atoms," *The J. Physical Chem. A*, vol. 101, no. 28, pp. 5111-5116, 1997.
- [38] N. J. Tustison et al., "N4ITK: Improved N3 bias correction," IEEE
- *Trans. Med. Imag.*, vol. 29, no. 6, pp. 1310–1320, Jun. 2010. [39] M. J. Krabbe-Hartkamp *et al.*, "Circle of willis: Morphologic variation on three-dimensional time-of-flight MR angiograms," Radiology, vol. 207, no. 1, pp. 103-111, 1998.
- F. Mut, S. Wright, G. A. Ascoli, and J. R. Cebral, "Morphometric, geographic, and territorial characterization of brain arterial trees, Int. J. Numer. Methods Biomed. Eng., vol. 30, no. 7, pp. 755–766, 2014.
- [41] V. N. Kornienko and I. N. Pronin, Diagnostic Neuroradiol. Berlin, Germany: Springer, 2009
- [42] E. K. Noch, R. Ramakrishna, and R. Magge, "Challenges in the treatment of glioblastoma: Multisystem mechanisms of therapeutic resistance," World Neurosurgery, vol. 116, pp. 505-517, 2018.
- V. A. Cuddapah, S. Robel, S. Watkins, and H. Sontheimer, "A neurocentric perspective on glioma invasion," Nature Rev. Neurosci., vol. 15, no. 7, 2014, Art. no. 455
- [44] V. N. Rajapakse, S. Herrada, and O. Lavi, "Phenotype stability under dynamic brain-tumor environment stimuli maps glioblastoma pro-
- gression in patients," *Sci. Advances*, vol. 6, 2020, Art. no. eaaz4125. [45] S. D. Wang *et al.*, "EphB2 receptor controls proliferation/migration dichotomy of glioblastoma by interacting with focal adhesion kinase," Oncogene, vol. 31, no. 50, pp. 5132–5143, 2012.
- [46] K. R. Swanson, E. C. Alvord Jr, and J. Murray, "A quantitative model for differential motility of gliomas in grey and white matter," Cell Proliferation, vol. 33, no. 5, pp. 317-329, 2000.
- [47] N. J. Mickevicius et al., "Location of brain tumor intersecting white matter tracts predicts patient prognosis," J. Neuro-Oncol., vol. 125, no. 2, pp. 393-400, 2015.
- M. Esmaeili, A. L. Stensjøen, E. M. Berntsen, O. Solheim, and I. Reinertsen, "The direction of tumour growth in glioblastoma patients," Sci. Reports, vol. 8, no. 1, pp. 1-6, 2018.
- J. E. Villanueva-Meyer, M. C. Mabray, and S. Cha, "Current clinical
- brain tumor imaging," *Neurosurgery*, vol. 81, no. 3, pp. 397–415, 2017. [50] M. Iv, B. C. Yoon, J. J. Heit, N. Fischbein, and M. Wintermark, "Current clinical state of advanced magnetic resonance imaging for brain tumor diagnosis and follow up," Seminars Roentgenol., vol. 53, no. 1, pp. 45-61, 2018.
- [51] M. Lim, Y. Xia, C. Bettegowda, and M. Weller, "Current state of immunotherapy for glioblastoma," Nat. Rev. Clin. Oncol., vol. 15, no. 7, 2018, Art. no. 422.
- F. Lieberman, "Glioblastoma update: Molecular biology, diagnosis, treatment, response assessment, and translational clinical trials," F1000Research, vol. 6, 2017, Art. no. 1892.



Junxi Zhu received the master's degree in mechanical engineering from the University of Maryland, College Park, Maryland. He is currently working at the Integrative Cancer Dynamics group at CCR/NCI/NIH, under the supervision of Dr. Orit Lavi. He research interest includes biomedical image analysis. He developed the methods, implemented all code, summarized the results, figures, and tables in this manuscript.



Spencer Teolis received the BSc degree in computer science, from the University of Maryland, Baltimore County (UMBC), Baltimore, Maryland. He is currently working at the Integrative Cancer Dynamics group at CCR/NCI/NIH, under the supervision of Dr. Orit Lavi. His research interests include deep learning methods and biomedical image analysis. He contributed the MRIs registration and tumor segmentations in this manuscript.



Pierre-Emmanuel Jabin is currently the director of the Center for Scientific Computation and Mathematical Modeling (CSCAMM) and a professor with the Department of Mathematics, University of Maryland (UMD), College Park, Maryland. He proposed some of the mathematical approaches and advised on their implementations in this manuscript.



Nadia Biassou is currently a staff clinician and attending neuroradiologist with the Department of Radiology and Imaging Sciences, Clinical Center, NIH, Bethesda, Maryland. She is also the director at NIH Clinical Neuroradiology Clerkship. She contributed to the clinical interpretation of both neuroimaging and computational simulations in this article.



Orit Lavi is currently the head of the Integrative Cancer Dynamics group at CCR/NCI/NIH. Her research program emphasizes an interdisciplinary theoretical approach to integrate the fields of mathematical oncology with data science, translating basic science into medicine using theories and methods from mathematics, physics, computer science and statistics. She conceived the project, designed the experiments, developed the methods, analyzed the data, and summarized the results in this article.



Amy Tabb is currently a research scientist/engineer, and a principal investigator, working on computer vision and robotics problems in the agricultural domain, at the United States Department of Agriculture, Agricultural Research Service, Appalachian Fruit Research Station. She contributed the curve skeletonization algorithm code in this manuscript.

▷ For more information on this or any other computing topic, please visit our Digital Library at www.computer.org/csdl.